Indian Journal of Pure & Applied Physics
Vol. 64, October 2026, pp. 1137-1147
DOI: 10.56042/ijpap.v64i10.31855

Analysis of Joule Heating and Activation Energy on Casson Nanofluid Flow in an Inclined Sheet-Numerical Study

A Magesh[a*], R Chitra[a] & P Tamizharasi[b]

[a]Department of Mathematics, Sri Sai Ram Engineering College, Chennai, Tamilnadu 600 044, India

[b]Department of Mathematics, Easwari Engineering College, Chennai, Tamilnadu 600 089, India

Received: 22nd May 2026; accepted: 20th August 2026

This investigation focused the influence of activation energy and Joule heating on the Casson nano fluid in an inclined sheet. The use of ohmic heating in a viscoelastic nanofluid is essential to making this work more distinctive. The flow behaviour of nanofluids and heat transport characteristics are greatly impacted by this ohmic heating in more efficient energy transfer mechanisms. Governing flow equations of non-Newtonian nanofluids flow through an inclined sheet are formulated. In addition of heat absorption parameter, Thermal radiation parameter and, magnetic field are considered. The governing Partial differential equations like temperature, velocity, and concentration equations are transformed into nonlinear Ordinary differential equation by utilizing suitable similarity variables. The 4th order Runge-Kutta method with shooting technique is used to numerically solve the coupled Ordinary differential equations that describe the momentum, heat and mass transfer. Finally, the influence of fluid parameter is discussed in details through the graphical illustrations. The results are tabulated based on numerical data compared to fundamental engineering formulas such as skin friction coefficient, Nusselt, and Sherwood numbers. The results were compared to previously published results and determined to be a good match. Moreover, the current finding shows that, the fluid velocity decreases when the Hartmann number, Darcy number, Casson parameter, and inclination angle increases.

Keywords: Casson nanofluid, Activation energy, Magnetic field, Thermal radiation

1 Introduction

The energy desire to provide a chemical or nuclear system of latent reactants in order to begin a chemical reaction, a nuclear reaction, or other physical phenomena is known as activation energy in chemistry and physics. It is represented by the sign (Ea) and measured in kilojoules/mol. The Swedish chemist Arrhenius[1] first used the phrase in 1889. The combined convective Darcy-Forchheimer movement of Casson liquid with gyrotactic microorganisms in a porous cylinder surface was analyzed[2]. Theoretical analysis of Darcy-Forchheimer transport of Maxwell nano liquid across a porous stretched sheet[3]. They also considered Arrhenius activation energy and Nield boundary conditions. Impact of activation energy through various flow geometries is presented in[4-9].

Researchers and scientists have been paying close attention to the movement of non-Newtonian nanomaterials in a decade, due to their practical applications in several scientific and technical domains. Casson liquid is classified as a non-Newtonian liquid because of its rheological features. It exhibits elastic solid behaviour, with little shear strain and no flow above a critical shear stress. However, flow happens in Casson liquid when the yield stress is exceeded by the shear force. This with zero shear force limitations is used to examine the traditional distinction of higher shear thinning. Human blood, orange juice, soup, honey and tomato sauce are a few well-known examples of fluids that exhibit Casson fluid behaviour. The combined consequences of a magnetic field, wall slip, and Joule heating on the electro-osmotic peristaltic motions of a conducting Casson liquid in the spinning channel with heat transfer were examined[10]. Under the influence of a magnetic field, the Casson liquid flow in an annular region of spinning cylinders was examined[11]. The movement of an fluctuating natural convection in which heat and mass transfer grainy non-Newtonian Casson liquid via a vertical plate was studied[12]. The effects of thermophoresis and Brownian motion on magnetohydrodynamic 3 dimensional Casson nanofluid slip motion on an exponentially extending sheet were looked[13]. The numerical solution of the heat source effect on an unstable MHD Casson fluid flow across a vertical oscillating plate in a porous

*Corresponding author: E-mail: mageshmaths86@gmail.com

medium was examined[14]. The mass and heat distributions for the Casson liquid dynamics over porous media across diminishing walls under Lorentz force and heat source/sink, were investigated[15]. The elaborate dynamics of Hall current, radiation, magnetic fields, and rotating buoyancy in a Casson fluid medium were studied[16]. A few studies on Casson nanofluid[17-19].

The movement of liquid over a porous media is governed by Darcy's law. Based on his studies of water flow across sand beds, French engineer Darcy developed this law in 1856. However, when boundary implications and inertial influences lead to higher flow rates, this method exhibits a deceptive trend. Later, Forchheimer developed the idea of the Darcian pattern by explaining the behaviour of boundary layer and inertia flow using the velocity element[20]. The flows over porous surfaces are of interest to many researchers because to their extensive uses in geothermal sciences and industry, like nuclear waste disposal, water flow in reservoirs, underground water systems, and energy storage units[21-25].

In many industrial operations, the quickest heat transfer is the most important factor. Fluids are the most prevalent way that heat is transferred. The fluids with the highest thermal conductivity are the best candidates for heat transportation. Fluids, however, lack the necessary greater heat conductivity. In order to improve the targeted fluids' thermal conductivity, a number of strategies have been used. The most recent methodology is nanoparticle dispersion (mono-, di-, and ternary). Nanofluids are defined as fluids containing nanoscale particles. Compared to the base liquid, the nano liquids have a larger thermal conductivity. Liquids containing nanoparticles allow for optimal heat transport due to the fluid's increased thermal conductivity. This remarkable development in heat transport motivated scientists, researchers, engineers, and physicists to study many facets of heat transfer in nanofluids. Some studies of nano fluid is listed in the[26-28].

Heat transfer is an essential component of many processes in industry and daily life. Heat transfer is widely used in automobiles, spray painting, mechanical operating systems, thermal and cooling processes, heat pipes, chemical and biological processes, HVAC (Heating, Ventilation, and Air Conditioning), electronics devices, thin film coating, heat exchangers, etc. Several methods have been employed to investigate the mechanism of heat transmission in fluids. Both theoretical and experimental approaches have already been applied. However, the least expensive and most cost-effective approach are theoretical approaches based on mathematical modeling. A theoretical approach has been widely employed in the past few decades. Looked on the use of Joule and heat production features in central composite design modeling to optimize the rate of thermal transfer in the viscoplastic nanomaterials. Many studies have been published on this topic[29-34].

Magnetohydrodynamics (MHD), also known as magneto-hydro fluid dynamics, is the study of fluid motion caused by two orthogonal magnetic and electric fields. Examples of these liquids include liquid metals, plasma generation, Micro-electro mechanical system (MEMs), solar collectors, and salt water or electrolytes. Riche first noticed MHD flow in 1832. He suggested that when an electrically conducting liquid is present, applying two orthogonal electric and magnetic fields creates a Lorentz force along the duct. Hannes Alfvén won the Nobel Prize in 1970 for developing the basic concepts of MHD flow in 1940. Studies on this flow started and are still ongoing after the general ideas of this flow were introduced. Because of its varied properties, this phenomenon has been applied in a variety of fields. Scientists have studied MHD in various domains, including hydrogen combustion, plasma physics, liquid metal flow engineering, astrophysics, geophysics, high electric conductivity fluid pumping and nuclear reactors. The Navier-Stokes equations of Maxwell's equations and fluid dynamics of electromagnetism are combined to provide a set of equations that characterizes MHD. These differential equations can be solved numerically or analytically[35-38].

From the Existing literature, the flow of Casson nano fluid has not focussed on the impact of activation energy in the inclined stretching sheet. Therefore, the present analysis focused the above-mentioned gap. The governing equations of non-Newtonian hybrid nanofluids are formulated. The set of present partial differential equations are converted into nonlinear ordinary differential equations utilising the suitable similarity variables. For a good comparison, the system of these transformed expressions is numerically solved using bvp4c and deciphered using the shooting technique. Quantitative examination of key parameters such skin friction, temperature, concentration, velocity, and Sherwood numbers is a great resource for engineers and

researchers working in the field. The findings have significant implications for engineering applications that use heat and mass transfer, including cooling systems and material processing. This paper advances the discipline and provides useful insights for both theoretical investigation and application by clarifying the impacts of thermal radiation and magnetic fields on MHD applications in a variety of industrial scenarios.

2 Methodology

2.1 Mathematical Formulation

The presence of the porosity parameter, Brownian motion and Thermophoresis parameter impact are taken into consideration in the MHD Casson liquid of viscous, incompressible, electrically conducting liquid through an inclined sheet moving at an unvarying velocity with activation energy and radiation. The velocity $U_w = px^{\frac{n-1}{2}}, (p > 0)$ of the surface differ from the track of the x-direction and the velocity in the y-direction is $v = v_w$. Additionally, the current flow area is positive $(y > 0)$. Furthermore, this sheet is frequently executed with the equivalency $B(x) = B_0 x^{\frac{n-1}{2}}$ by a magnetic strength that is in the y-axis pathway is shown in Fig. 1. The corresponding magnetic field attracts the electrically conducting liquid. It should be mentioned that the forced magnetic field gets closer to zero if the Reynolds number is extremely low. The wall has been broadened while the base remains fixed by applying two opposing and indistinguishable forces in the x-axis direction. In addition to suction and dissipation, the analysis considers the effects of heat generation, Joule heating, and porous media. Assuming that the Casson fluid's rheological Eq.[17,18];

$$\tau = \tau_0 + \mu a * \quad \ldots (1)$$

$$\tau_{ij} = \begin{cases} 2\left(\mu_B + \frac{p_y}{\sqrt{2\pi}}\right) e_{ij}, \pi > \pi_c \\ 2\left(\mu_B + \frac{p_y}{\sqrt{2\pi_c}}\right) e_{ij}, \pi < \pi_c \end{cases}, \quad \ldots (2)$$

where, p_y, μ_B, π_c are fluid yield stress, Casson fluid's dynamic viscosity, critical value of $\pi (= e_{ij} e_{ij})$

$$e_{ij} = \frac{1}{2}\left(\frac{\partial v_i}{\partial x_j} + \frac{\partial v_j}{\partial y_i}\right) \quad \ldots (3)$$

where e_{ij} is the deformation rate component.

Important characteristics of a Casson fluid consist of;

(i) Shear-thinning characteristic

Casson liquids exhibit shear-thinning characteristics, which indicates that their viscosity declines as the shear rate grows. Conversely, Newtonian fluids have a constant viscosity independent of shear rate variations.

(ii) Yield stress

The minimum shear stress needed to start flow is indicated by the yield stress of Casson fluids. The fluid is either stagnant or exhibits solid-like behaviour below this threshold. Fluid starts to flow when the yield stress is surpassed, and as the shear rate rises, its viscosity lowers.

(iii) Nonlinear relationship

In a Casson fluid, the relationship between shear rate and shear stress is nonlinear. The Casson equation describes this nonlinearity and is used to quantitatively model the behaviour of the fluid.

In radiative heat transfer analysis, the Rosseland approximation is frequently employed, particularly for optically thick media. It makes radiative heat transfer computations easier in a participating medium with considerable radiation absorption and emission. The Rosseland approximation assumes that the radiative flux was determined by temperature gradient rather than temperature itself. This approach is valid for optically thick or dense media, which contain a large number of absorbing and emitting particles. The Rosseland approximation is especially useful while scattering and absorption phenomena are

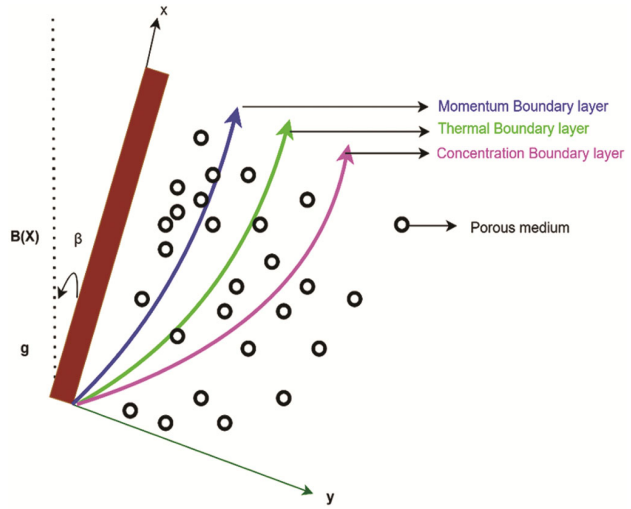


Fig. 1 — Flow geometry

the primary elements controlling radiative transmission. Mathematically, q_r (radiative heat flux) can be presented as follows[8];

$$q_r = -\frac{4\sigma^s \partial T'^4}{3k*\partial y} \quad . \quad \ldots (4)$$

In Eq. (4), expand T'^4 about T_0 as the Taylor series after neglective higher-order terms

$$T'^4 \approx 4T(T_1 - T_0)^3 - 3(T_1 - T_0)^4 \quad \ldots (5)$$

The present flow problem is modeled by the system of equations provided by[39];

$$\frac{\partial u}{\partial x} + \frac{\partial v}{\partial y} = 0 \quad \ldots (6)$$

$$u\frac{\partial u}{\partial x} + v\frac{\partial u}{\partial y} = \upsilon\left(1+\frac{1}{\alpha}\right)\frac{\partial^2 u}{\partial y^2} - \frac{\sigma_s B^2(x)}{\rho_f}u - \frac{\upsilon}{k}u + \left(g\beta^T(T-T_\infty) + g\,\beta^c\,(C-C_\infty)\right)cos\beta \quad \ldots (7)$$

$$v\frac{\partial T}{\partial y} + u\frac{\partial T}{\partial x} = \gamma\frac{\partial^2 T}{\partial y^2} + \frac{(\rho c)_p}{(\rho c)_f}\left[\frac{D_T}{T_\infty}\left(\frac{\partial T}{\partial y}\right)^2 + D_B\frac{\partial T}{\partial y}\frac{\partial C}{\partial y}\right] + \frac{\upsilon}{c_p}\left(1+\frac{1}{\alpha}\right)\left(\frac{\partial u}{\partial y}\right)^2$$

$$+\frac{\sigma_1 B^2(x)}{(\rho c)_f}u^2 - \frac{1}{(\rho c)_f}\left(\frac{\partial q_r}{\partial y}\right) + \frac{1}{(\rho c)_f}Q_S(T-T_\infty) \quad \ldots (8)$$

$$u\frac{\partial C}{\partial x} + v\frac{\partial C}{\partial y} = D_B\left(\frac{\partial^2 C}{\partial y^2}\right) + \frac{D_T}{T_\infty}\left(\frac{\partial^2 T}{\partial y^2}\right) - k_r^2(C-C_\infty)\left(\frac{T}{T_\infty}\right)^m \exp\left(-\frac{E_a}{kT}\right) \quad \ldots (9)$$

where $B(x) = B_0 x^{\frac{n-1}{2}}$ is the inconstant magnetic field, γ denotes thermal diffusivity, $T_\infty, \rho c_f$, $\rho c_p, D_B, Q_S, \sigma_1, \upsilon, k^*, C$ are the ambient temperature, fluid and particles specific heat capacity , Brownian diffusion coefficient, heat source parameter, electrical conductivity, kinematic viscosity, mean absorption coefficient, concentration, v and u are the velocities, T is the temperature, D_T defines thermophoretic diffusion coefficient, $k_r^2(C-C_\infty)\left(\frac{T}{T_\infty}\right)^m \exp\left(-\frac{E_a}{kT}\right)$ is the Arrhenius expression. Using the Eqs. (4) and (5), Eq. (8) becomes

$$u\frac{\partial T}{\partial x} + v\frac{\partial T}{\partial y} = \gamma\frac{\partial^2 T}{\partial y^2} + \frac{(\rho c)_p}{(\rho c)_f}\left[\frac{D_T}{T_\infty}\left(\frac{\partial T}{\partial y}\right)^2 + D_B\frac{\partial C}{\partial y}\frac{\partial T}{\partial y}\right] + \frac{\upsilon}{c_p}\left(1+\frac{1}{\alpha}\right)\left(\frac{\partial u}{\partial y}\right)^2 + \frac{\sigma_s B^2(x)}{(\rho c)_f}u - \frac{\upsilon}{k}u + \frac{1}{(\rho c)_f}\left[\frac{16\sigma^*}{3k^*}\frac{\partial}{\partial y}\left(\frac{T^3\partial T}{\partial y}\right)\right] + \frac{1}{(\rho c)_f}Q_S(T-T_\infty) \quad \ldots (10)$$

The similarity variables are;

$$\Psi = \sqrt{\frac{2p\upsilon}{n+1}}x^{\frac{n-1}{2}}f(\eta), \eta = \sqrt{\frac{n+1}{2\upsilon}}x^{\frac{n-1}{2}}, v = -\frac{\sqrt{p\upsilon(n-1)}}{2}x^{\frac{n-1}{2}}\left[f(\eta) + \frac{n-1}{n+1}n\,f'(\eta)\right]$$
$$u = px^{\frac{n-1}{2}}f'(\eta), \ \sigma = \frac{C-C_\infty}{C_w-C_\infty}, \theta = \frac{T-T_\infty}{T_w-T_\infty} \quad \ldots (11)$$

and the stream functions are $u = \Psi_x, v = -\Psi_y$

The partial differential equations are transformed to the following ordinary differential equations using Eq. (12);

$$\left(1+\frac{1}{\alpha}\right)f''' + ff'' - (EC\,M + Da)f' - \frac{2n}{n+1}f'^2 + \frac{2}{n+1}(Gm\sigma + Gr\theta)cos\beta = 0 \quad \ldots (12)$$

$$\left(\frac{3+4Nr}{3}\right)\theta'' + \Pr\left[f\theta' + Nt\theta'^2 + Nb\theta'\sigma' + Ec\,M\,f'^2 + \left(1+\frac{1}{\alpha}\right)Ecf''^2 + Q\theta\right] = 0 \quad \ldots (13)$$

$$\sigma'' + \Pr Lef\sigma' + \frac{Nt}{Nb}\theta'' - PrLe\sigma_1(1+\Omega\theta)^m \exp\left[-\frac{E}{1+\Omega\theta}\right]\sigma = 0 \quad \ldots (14)$$

The modified initial and boundary conditions are provided by[39];

$$f(\eta) = S, f'(\eta) = 1, \theta(\eta) = 1, \sigma(\eta) = 1 \ \ at\ \eta = 0$$
$$f'(\eta) = 0, \theta(\eta) = 0, \sigma(\eta) = 0\ as\ \eta \to 0 \quad \ldots (15)$$

The non-dimensional parameters are as follows[40];

$$Gr = \frac{g\beta^T(T_w-T_\infty)}{p^2x^{2n-1}}, Gm = \frac{g\beta^C(C_w-C_\infty)}{p^2x^{(2n-1)}}, M = \frac{2\sigma_s B_0^2}{p\rho_f(n+1)},$$
$$\Omega = \frac{T_w-T_\infty}{T_\infty}, E = \left(\frac{E_a}{kT_\infty}\right) \ Nt = \frac{(\rho c)_p D_T(T_w-T_\infty)}{\upsilon(\rho c)_f}, Pr = \frac{\upsilon}{\gamma},$$
$$\gamma = \frac{k}{(\rho c)_f}, Kc = \frac{2xkr}{(n+1)U_w}, Ec = \frac{Uw^2}{(T_w-T_\infty)_{cp}}, Le = \frac{\gamma}{D_B}, \sigma_1 = \left(\frac{k_r^2}{\alpha}\right)$$
$$Nb = \frac{(\rho c)_p D_B(C_w-C_\infty)}{\upsilon(\rho c)_f}, \ D_a = \frac{\upsilon}{pk}, \ S = -\frac{\upsilon_w}{\left(\frac{\sqrt{p(n+1)\upsilon}}{2}x^{\frac{n-1}{2}}\right)},$$
$$Q = \frac{2xQ_S}{(\rho c)_f(n+1)U_w}, Nr = \frac{4\sigma^* T_\infty^3}{k^*k}$$

$$Da = \left(\frac{\upsilon}{\rho_k}\right), \ k = k_\infty\left(1+\varepsilon\,\frac{T-T_\infty}{T_w-T_\infty}\right), \ Re_x = \frac{U_w x}{\upsilon}, M = \frac{(2\sigma_s\beta_0^2\,U_w)}{(p\rho_f(T_w-T_\infty)C_p(n+1))} \quad \ldots (16)$$

here $E, Nb, Pr, Nr, Nt, Le, M, \Omega$ are activation energy parameter, Brownian motion, Prandtl number, thermal radiation, thermophoresis parameter, Lewis number, magnetic parameter, temperature ratio parameter, σ_1, Da, k, Re, Ec, Q, S, m denotes electrical conductivity, porosity parameter, thermal conductivity, local Reynolds number, Eckert number, heat source parameter, suction parameter and fitted

rate constant respectively. The definitions of C_f, Nu and Sh are as follows;

$$C_f = \frac{\mu_\beta}{\rho U_w^2}\left(1+\frac{1}{\alpha}\right)\left(\frac{\partial u}{\partial y}\right)_{y=0}$$

$$Nu_x = \frac{xq_w}{k(T_w - T_\infty)}$$

$$Sh_x = \frac{xq_m}{D_B(C_w - C_\infty)} \quad \ldots (17)$$

where q_w and q_m are heat flux, mass flux respectively, and it is expressed as;

$$q_w = \left[-\left(k+\frac{16\sigma^S T_\infty^3}{3k^*}\right)\left(\frac{\partial T}{\partial y}\right)\right]_{y=0}$$

$$q_m = -D_m\left(\frac{\partial C}{\partial y}\right)_{y=0}$$

The dimensionless engineering quantities can be simplified using the similarity parameters as presented below[39];

$$Re_x^{\frac{1}{2}} Sf_x = \sqrt{\frac{2}{1+n}}\left[1+\frac{1}{\alpha}\right]f''(0)$$

$$Re_x^{-\frac{1}{2}} NU_x = -\sqrt{\frac{2}{n+1}}\left[\frac{3+4Nr}{3}\right]\theta'(0) \quad \ldots (18)$$

$$Re_x^{-\frac{1}{2}} Sh_x = -\sqrt{\frac{2}{n+1}}\sigma'(0)$$

2.2 Numerical Computations

The MATLAB software function bvp4c approach has been used to numerically solve the set of non-similar Eqs. (12) – (14) along with supporting boundary conditions Eq. (15). The final system is transformed into an Initial value problem and reduced to a series of first ordinary differential equations are as follows;

$$\Gamma_1 = f, \Gamma_2 = f', \Gamma_3 = f'', \Gamma_4 = \theta, \Gamma_5 = \theta', \Gamma_6 = \sigma, \Gamma_7 = \sigma'$$

$$\Gamma_3' = \frac{1}{\left(1+\frac{1}{\alpha}\right)}\left[(M+Da)\Gamma_2 + 2\left(\frac{n}{n+1}\right)\Gamma_2{}^2 + \left(\frac{2}{n+1}\right)(Gm\Gamma_6 - Gr\Gamma_4 cos(\beta) - \Gamma_1\Gamma_3\right]$$

$$\Gamma_5' = -\left[\left(\frac{3Pr}{3+4Nr}\right)\left(\left(\Gamma_1\Gamma_5 + Nt\Gamma_5^2 + Nb\Gamma_5\Gamma_7 + MEc\Gamma_2{}^2 + Q\Gamma_4 + \left(1+\frac{1}{\alpha}\right)Ec\Gamma_3^2\right)\right)\right]$$

$$\Gamma_7' = -\left\{\left[\left(\frac{Nt}{Nb}\right)\left(\frac{-3Pr}{3+4Nr}\right)\right]\left[\Gamma_1\Gamma_5 + Nt\Gamma_5^2 + Nb\Gamma_5\Gamma_7 + MEc\Gamma_2{}^2 + Q\Gamma_4 + \left(1+\frac{1}{\alpha}\right)Ec\Gamma_3^2\right]\right\} - LePr\Gamma_1\Gamma_7 + LePr\sigma_1(1+\Omega\Gamma_4)^m exp\left(\frac{-E}{1+\Omega\Gamma_4}\right)\Gamma_6$$

The boundary conditions are as follows;

$$\Gamma_1 = 1, \Gamma_2 = 1, \Gamma_4 = 1, \Gamma_6 = S, at\ \eta = 0,$$
$$\Gamma_2 \to 0, \Gamma_4 \to 0, \Gamma_6 \to 0\ as\ \eta \to 0$$

3 Results and Discussion

The impacts of several relevant parameters incorporated in the problem on the nanofluid velocity (f'), temperature (θ) and concentration (σ) are graphically depicted in order to understand the physical insight of the modelled situation. The arithmetic computations were performed by taking into account the constant values of the many included parameters in the flow field, which are clearly depicted in the graphs. Additionally, Tables (1), (2) and (3) present and analyse the effects of important words on the physical quantities of concern, such as Skin friction coefficient (C_f), Nusselt number (Nu) and Sherwood number (Sh).

3.1 Velocity Distribution

The impact of Hartmann number (M) on the velocity profile (f') is seen in Fig. 2. The velocity

Table 1 — Variations of skin friction coefficient

Da	M	n	α	m	Cf
0.5	1	0.8	1.2	0.5	-1.137921
0.6					-1.161435
0.7					-1.184516
	1.1				-1.207148
	1.2				-1.22939
	1.3				-1.251259
		0.9			-1.260449
		1			-1.268664
		1.1			-1.276052
					-1.298899
			1.4		-1.319506
					-1.338193
					-1.338129
				0.7	-1.338065
				0.8	-1.337999

Table 2 — Variations of Nusselt number

Nr	Q	E	m	Ec	Nu
2	0.2	0.2	0.5	0.1	2.281201
2.1					1.835958
2.2					1.833022
	0.3				1.854617
	0.4				1.876677
	0.5				1.899231
		0.3			1.859668
		0.4			1.821807
		0.5			1.785594
			0.6		1.805779
			0.7		1.826531
			0.8		1.847862
				0.2	1.894769
				0.3	1.941634
				0.4	1.988457

Table 3 — Variations of sherwood number

Le	Nt	Nb	σ_1	Ω	Sh
3	0.3	0.4	0.6	0.2	1.642818
3.1					1.666645
3.2					1.690143
	0.4				1.864248
	0.5				1.965599
	0.6				2.067772
		0.1			2.351227
		0.2			1.910793
		0.3			1.76373
			0.7		2.117564
			0.8		2.166418
			0.9		2.214353
				0.3	2.237856
				0.4	2.260087
				0.5	2.281201

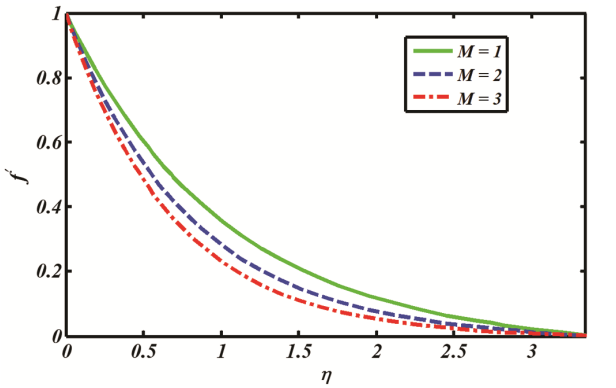


Fig. 2 — Velocity profile for M with $Nr = 0.5, \beta = \frac{\pi}{4}; Nt = 0.2; Nb = 0.4, Le = 4,\ Ec = 1, Pr = 1.9, Q = 0.1, \alpha = 1.2, n = 1\ S = 0.01, Gm = 0.1, Gr = 0.1, \sigma_1 = 1.2, \Omega = 0.8, E = 5, m = 0.5, Da = 2.1$

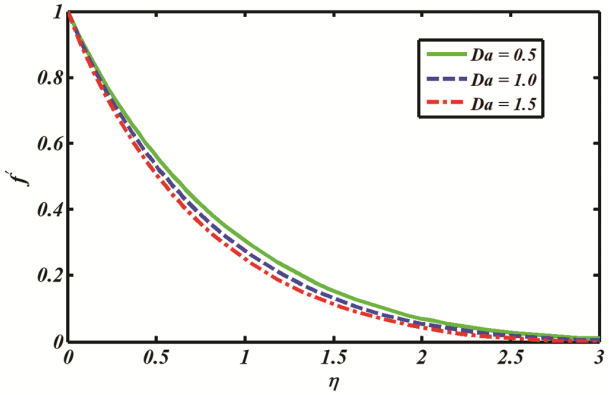


Fig. 3 — Velocity distribution for Da with $Nr = 2; \beta = \frac{\pi}{6}, Nt = 0.3, Nb = 0.4, Le = 4, Ec = 0.5, Pr = 6.7, Q = 1.2, \alpha = 1.2, n = 0.8, S = 0.01, Gm = 0.1, Gr = 0.1, \sigma_1 = 0.6, \Omega = 0.2, E = 0.2, m = 0.5, M = 1$

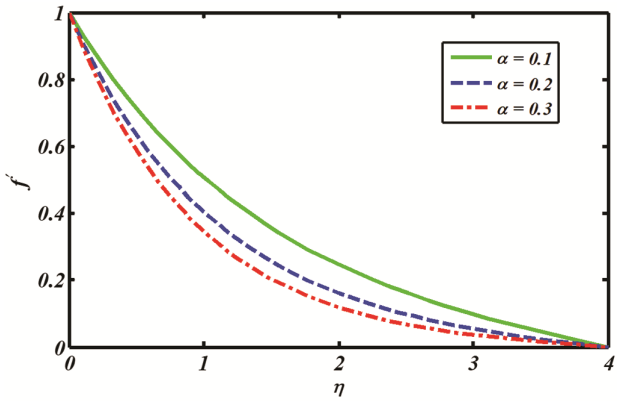


Fig. 4 — Velocity profile for α with $Nr = 0.5, \beta = \frac{\pi}{4}, Nt = 0.2, Nb = 0.4, Le = 4, Ec = 1, Pr = 1.9, Q = 0.1, Da = 2.1, n = 1, S = 0.01, Gm = 0.1, Gr = 0.1, \sigma_1 = 1.2, \Omega = 0.8, E = 5, m = 0.5, M = 2$

slows down when a transverse magnetic field is present because it creates a Lorentz force. So, the fluid motion decreases as Hartmann number M increases since the force slowing it down increases as well. The effect of permeability parameter on the velocity profile (f') is seen in Fig. 3. The number of porous spaces rises with Darcy number (Da), impeding the flow and reducing overall fluid mobility. When porosity parameter value enhances, the amount of porous in the substrate also enhances. Fluid cannot enter via these pores. It must thus make an effort to move through the permeable material. The fluid must progressively slow down at each step because its path is unclear. Thus, the flow rate decreases as Darcy number (Da) increases. Figure 4 placed the graphical illustrations of Casson fluid parameter α on the velocity region. From this figure,

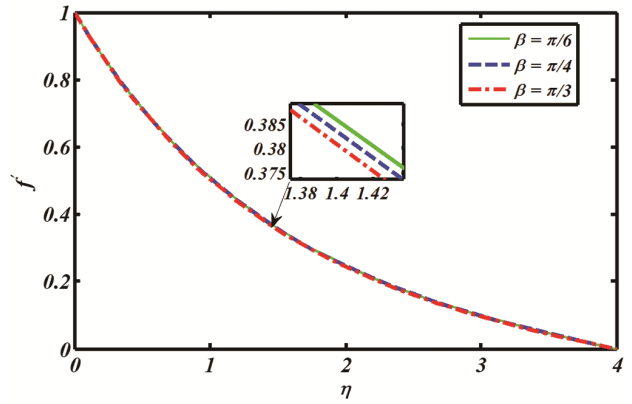


Fig. 5 — Velocity profile for β with $Nr = 0.5, \alpha = 0.1, Nt = 0.2, Nb = 0.4, Le = 4,\ Ec = 1, m = 0.5, Q = 0.1, Da = 2.1, n = 1, S = 0.01, Gm = 0.1, Gr = 0.1, \sigma_1 = 1.2, \Omega = 0.8, E = 5, M = 2, Pr = 1.9$

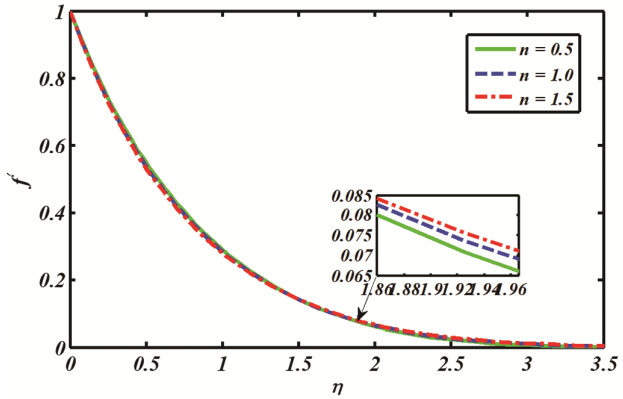


Fig. 6 – Velocity profile for n with $\alpha = 1.2, Le = 4,\ Ec = 0.5, Pr = 6.7, Q = 1.2, \beta = \frac{\pi}{4}, S = 0.01, Gm = 0.2, Gr = 0.1, \sigma_1 = 0{,}6, \Omega = 0.2, E = 0.2, m = 0.5, M = 1, Nt = 0.3, Nr = 2, Da = 0.8, Nb = 0.4$

it is noticed that a diminish in velocity due to the rising Casson fluid parameter (α). Higher plastic viscosity fluids are more resilient to deformation.

As a result, the flow becomes more resistant to changes in velocity and the velocity profile tends to become smoother. The influence of angle of inclination (β) to the vertical direction on the velocity profiles is depicted in Fig. 5. This figure shows that as the inclination angle (β) grows, the velocity slows down.

The influence of the buoyant force caused by thermal diffusion actually slows down as inclination angle (β) grows. Velocity profiles decrease as a result of the fluid's reduced driving force. The impact of a non-linear stretching parameter (n) on liquids velocity is depicted in Fig. 6. From this figure, increasing non-linear stretching parameter (n), slows down the fluid velocity when $\eta < 1.5$ and increasing

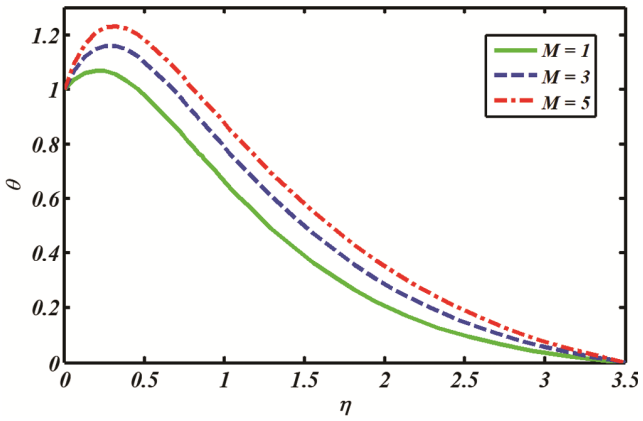


Fig. 7 — Temperature distribution for M with $Nr = 1.5, \beta = \frac{\pi}{4}, Nt = 0.1, Nb = 0.4,\ Le = 4, Ec = 0.5, Pr = 6.3, Q = 0.1, \alpha = 2, n = 0.8, S = 0.01, Gm = 0.1, Gr = 0.1, \sigma_1 = 0.2, \Omega = 0.8, E = 0.5, m = 0.5, Da = 2.1$

the fluid velocity when $\eta > 1.5$. Physically, by deepening the boundary stratum and snowballing the viscid drag, the nonlinear stretching parameter reduces the fluid velocity. This results in greater resistance to liquid motion near to elongating sheet. In the boundary layer domain, the result inclusively reduces the fluid velocity.

3.2 Temperature Distribution

The temperature distribution is affected by changes in the Hartmann and Eckert numbers (M and Ec), which appear as coefficients of factors associated with viscous dissipation and Joule heating. Both viscous dissipation and Joule heating generate heat, which contributes to the liquid's absolute energy. Hence, the distribution of temperature broadens, reducing the fluids' ability to transfer heat. Warm liquid has a poorer capacity to transmit heat than colder fluid. Because of this, viscous dissipation and Joule heating are detrimental to a fluid's thermal efficiency. Therefore, the fluid must be heat dissipative for the best possible heat transmission mechanism.

Figures 7 and 8 illustrate the increase in temperature distribution brought on by an increase in Hartmann number (M) and Eckert number (Ec) respectively. Figure 9 illustrates how radiation parameter (Nr) affects the temperature (θ). This is because a rise in thermal radiation results in a greater surface heat flow, which elevates the fluid's temperature in the boundary layer region. Also, thickness of the temperature boundary layer grows as radiation parameter Nr enhances.

Figure 10 illustrates the influence of Q on the temperature (θ). It shows that when heat absorption

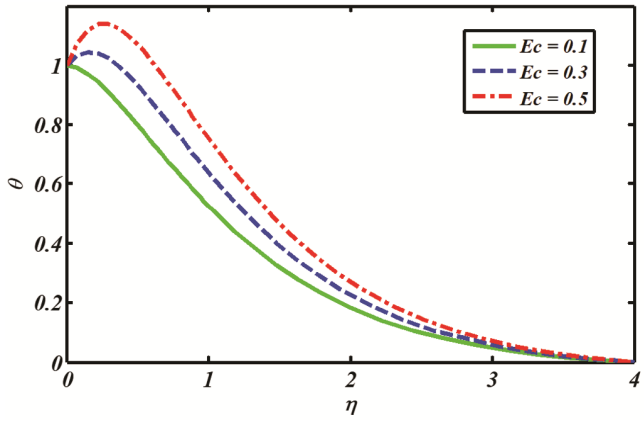


Fig. 8 — Temperature distribution for Ec with $Nr = 1.5, \beta = \frac{\pi}{4}, Nt = 0.1, Nb = 0.2,\ Le = 4, M = 2, Pr = 6.7, Q = 0.1, \alpha = 2, n = 2, S = 0.01, Gm = 0.1, Gr = 0.1, \sigma_1 = 2, \Omega = 0.8, E = 5, m = 0.5, Da = 2.1$

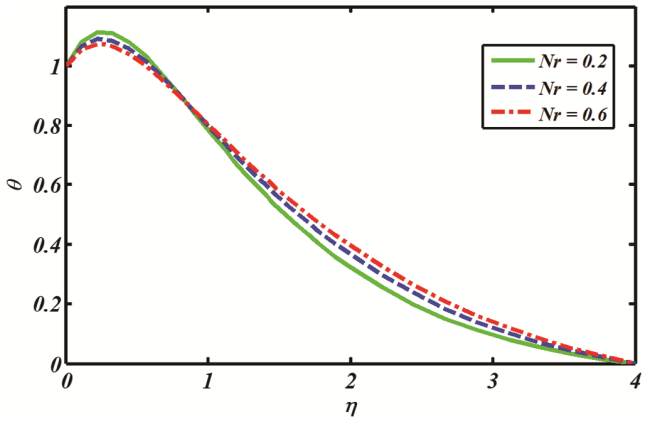


Fig. 9 — Temperature distribution for Nr with $Ec = 0.3, \beta = \frac{\pi}{4}, Nt = 0.1, Nb = 0.2, Le = 2, M = 2, Pr = 7, Q = 0.1, \alpha = 2, n = 1, S = 0.01, Gm = 0.1, Gr = 0.1, \sigma_1 = 0.6, \Omega = 0.2, E = 0.2, m = 0.5, Da = 2.1$

coefficient (Q) is increased as temperature (θ) increases. Furthermore, as heat absorption coefficient (Q) increases, the temperature boundary layer's thickness grows. It is expected that a higher temperature will normally be released into the working fluid during the heat-generating process. The heat production parameter raises the temperature profile as a result of this factor. Furthermore, exothermic chemical reactions may be responsible for an increase in temperature. Figures 11 and 12 show the characteristics of thermophoresis parameter (Nt) and Brownian motion parameter (Nb) in relation to the temperature curve. Temperature profile enhances against increasing the thermophoresis parameter (Nt) and Brownian motion parameter (Nb) estimates, as predicted. Brownian motion, from a

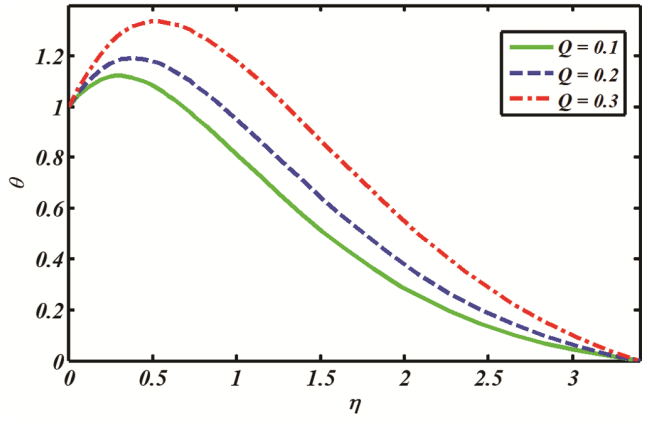


Fig. 10 — Temperature distribution for Q with $m = 0.5, \beta = \frac{\pi}{6}, Da = 0.8, Nb = 0.4,\ Gr = 0.1, M = 2, Pr = 6.7, Nr = 2, \alpha = 1.2, n = 0.8, S = 0.01, Gm = 0.1, Le = 4, \sigma_1 = 0.6, \Omega = 0.2, E = 0.2, Ec = 0.5, Nt = 0.3$

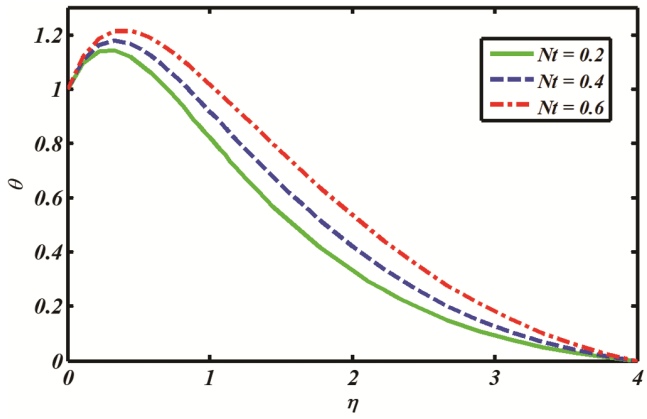


Fig. 11 — Temperature distribution for Nt with $Da = 2.1, \beta = \frac{\pi}{4}, Ec = 0.5, Nb = 0.3, Le = 4, M = 2, Nr = 0.1, \alpha = 2, n = 0.8, S = 0.01, Gm = 0.1, Gr = 0.1, \sigma_1 = 0.7,\ \Omega = 0.5, E = 0.5, m = 0.5, Q = 0.1, Pr = 2.3$

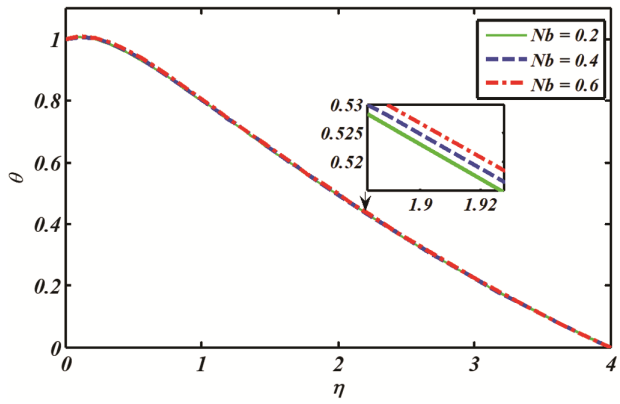


Fig. 12 — Temperature distribution for Nb with $Ec = 0.5, \beta = \frac{\pi}{4}, Q = 0.1, Nt = 0.3, Le = 4, M = 2, Pr = 2.4, Nr = 3, n = 0.8, S = 0.01, Gm = 0.1, Gr = 0.1, \sigma_1 = 0.8,\ \Omega = 0.5, E = 0.5, m = 0.5, Da = 2.1, \alpha = 2$

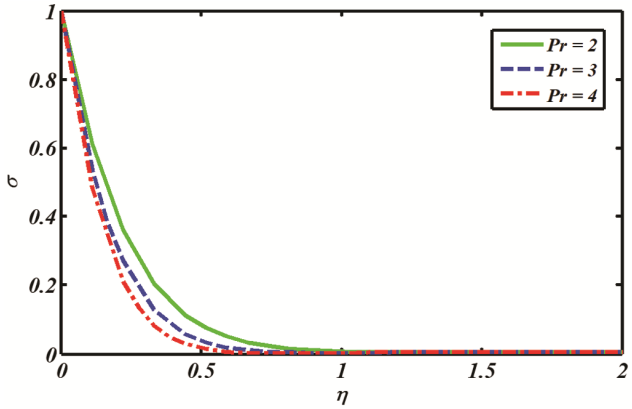


Fig. 13 — Concentration distribution for Pr with $Nt = 0.1, \beta = \frac{\pi}{4}, Ec = 0.5, Le = 4, Q = 0.1, M = 1, Nb = 0.2, Nr = 1.5, \alpha = 2, n = 2, S = 0.01, Gm = 0.1, Gr = 0.1, \sigma_1 = 2, \Omega = 0.8, E = 1.0, m = 0.5, Da = 0.8$

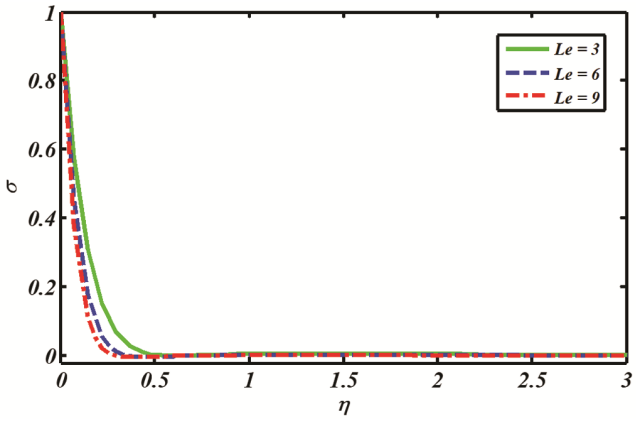


Fig. 14 — Concentration distribution for Le with $M = 2, \beta = \frac{\pi}{4}, E = 1.0, m = 0.5, Pr = 6.7, Ec = 0.5, Nb = 0.2, Nr = 1.5, \alpha = 2, n = 2, S = 0.01, Gm = 0.1, Gr = 0.1, \sigma_1 = 2, \Omega = 0.8, Q = 0.1, Nt = 0.1, Da = 2.1$

physical perspective, is the haphazard movement of liquid particles on a surface. This pattern of liquid particles consists of random oscillations in particle position within a working subdomain, followed by replacement with another subdomain. In the new closed volume, additional vibrations are used to track each replacement. The total of the kinetic energies of molecular vibrations, rotations, and random motions of the incredibly dense working liquid particles makes up the caloric component of the internal energy of the working liquid. As a result, temperature (θ) rises.

3.3 Concentration Distribution

The impact of Prandtl number (Pr) against the concentration (σ) is presented in the Fig. 13. The concentration profile diminishes with rise in Prandtl number (Pr). The concentration boundary layer

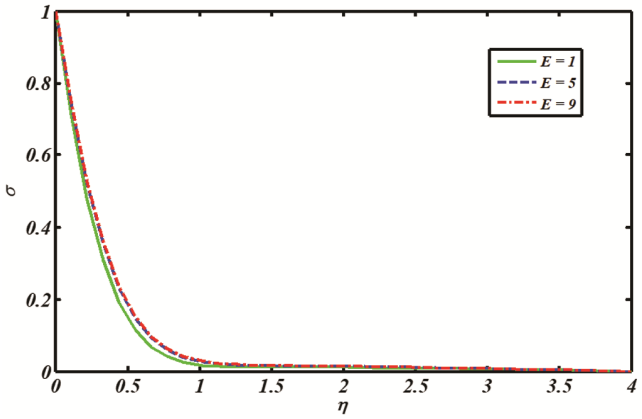


Fig. 15 — Concentration distribution for E with $Ec = 0.5, \beta = \frac{\pi}{4}, Q = 0.2, M = 2, Pr = 2.3, Nb = 0.2, Nr = 1.5, \alpha = 1.2, n = 0.8, S = 0.01, Gm = 0.1, Gr = 0.1, \sigma_1 = 0.3, \Omega = 0.8, Le = 4, m = 0.5, Da = 2.1, Nt = 0.1$

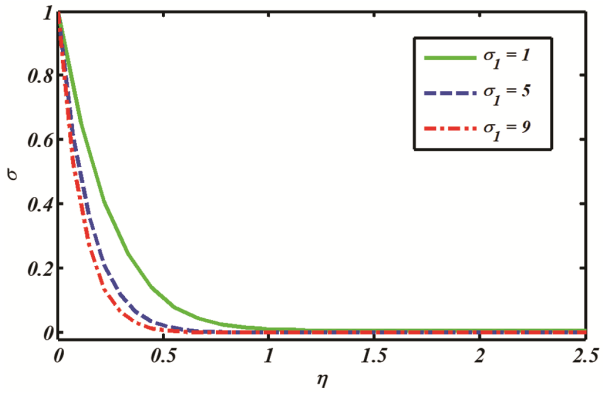


Fig. 16 — Concentration distribution for σ_1 with $Ec = 0.5, \beta = \frac{\pi}{4}, Q = 0.1, Nt = 0.1, Pr = 2.3, M = 2, Nb = 0.2, Nr = 1.5, \alpha = 2, n = 2, S = 0.01, Gm = 0.1, Gr = 0.1, E = 1.0, \Omega = 0.8, Le = 4, m = 0.5, Da = 2.1$

decreases as higher Prandtl values are generally associated with a lower concentration profile. Examining the change in Lewis number (Le) on the concentration profile (σ) is presented in Fig. 14. Decays in the concentration profile (σ) can be seen by increasing the Lewis number (Le). Since nanoparticle volume fraction increases with increasing Lewis number (Le). Thus, concentration and thickness layer diminished. Fig. 15 elaborates on the change in the concentration profile (σ) for various levels of activation energy (E). The velocity profile (f') improves as a result of the supplementing values of the activation energy (E). Reduced temperature and increased activation lead to a slower rate of reaction, which in turn increases the concentration of the solute.

Figure 16 illustrates the concentration profile's features as the electrical conductivity (σ_1) varies. The

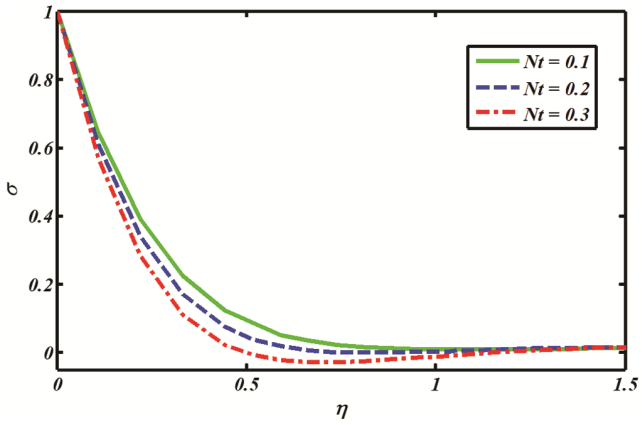


Fig. 17 — Concentration distribution for Nt with $Ec = 0.7, \beta = \frac{\pi}{4}, Q = 0.2, E = 0.2, Pr = 2.3, M = 2, Nb = 0.3, Nr = 0.2, \alpha = 2, n = 0.8, S = 0.01, Gm = 0.1, Gr = 0.1, \sigma_1 = 0.6, \Omega = 0.5, Le = 4, m = 0.5, Da = 21$.

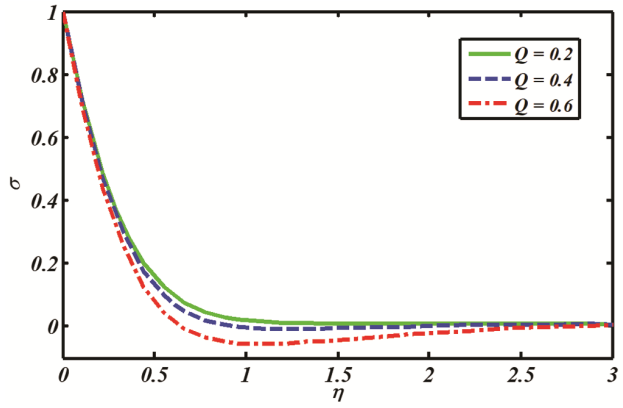


Fig. 18 — Concentration distribution for Q with $E = 1.0, \beta = \frac{\pi}{4}, Ec = 0.5, Nt = 0.1, Pr = 2.3, M = 2, Nb = 0.2, Nr = 1.5, \alpha = 2, n = 2, S = 0.01, Gm = 0.1, Gr = 0.1, \sigma_1 = 0.3, \Omega = 0.8, Le = 4, m = 0.5, Da = 2.1$

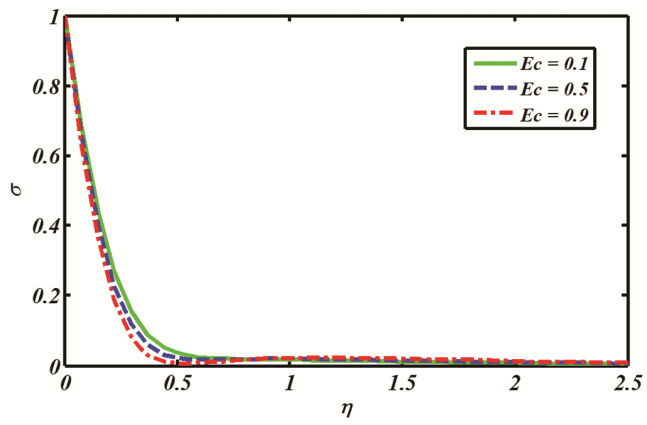


Fig. 19 — Concentration distribution for Ec with $E = 5, \beta = \frac{\pi}{4}, Q = 0.1, Nt = 0.1, Pr = 6.7, M = 2, Nb = 0.2, Nr = 1.5, \alpha = 2, n = 2, S = 0.01, Gm = 0.1, Gr = 0.1, \sigma_1 = 2, \Omega = 0.8, Le = 4, m = 0.5, Da = 2.1$

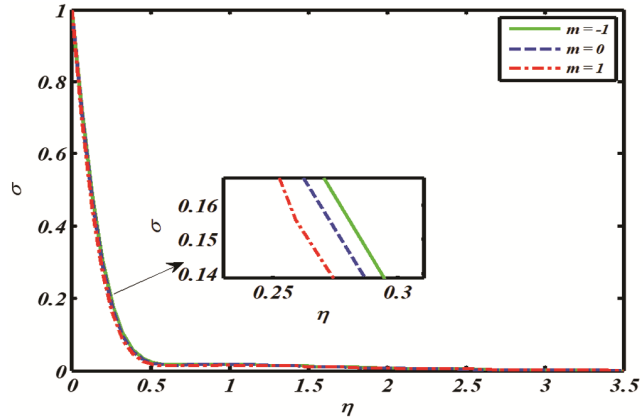


Fig. 20 — Concentration distribution for m with $E = 0.5, \beta = \frac{\pi}{4}, Ec = 0.5, Nt = 0.1, Pr = 6.7, M = 1, Nb = 0.2, Nr = 1.5, \alpha = 2, n = 0.8, S = 0.01, Gm = 0.1\ Gr = 0.1, \sigma_1 = 0.2, \Omega = 0.8, Le = 4, Q = 0.1, Da = 2.1$

solutal curves of the Casson nanofluid show a decreasing trend as the amount of the destructive chemical reaction limitation boosts ($\sigma_1 > 0$). The solutal rate actually decreases as a result of some solutal energy being destroyed by an enhance in the harmful chemical reaction restriction.

The effect of thermophoresis parameter (Nt) on the concentration profile (σ)is shown in Fig. 17. According to the figure, raising thermophoresis parameter (Nt) causes the concentration profile (σ) rise. This is because the concentration boundary layer thickens as a result of diffusion penetrating deeper into the fluid due to rising thermophoresis parameter (Nt) values. The impact of heat absorption coefficient Q against the concentration profile is presented in Fig. 18. This figure suggests that, the concentration (σ) diminishes to enhance the values of heat absorption coefficient (Q). A similar pattern can be seen in the concentration curve for Eckert number (Ec) in Fig. 19. This is because larger Eckert numbers can alter fluid viscosity, which in turn influences fluid concentration.

The concentration distribution fluctuations of fitted rate constant (m) is displayed in Fig. 20. As demonstrated in Fig. 20, a rising m is corresponding to a declining concentration profile. The current analysis is compared to the existing literature[38] of $f''(0)$for various M and $Gr = Gm = Da = \beta = 0, \alpha \to \infty$, which are shown in Table 4. The derived solution in this study is validated by looking at how it differs from earlier literature at the simplified condition, which increases trust in the accuracy of the result.

Table 4 — comparison result of $f''(0)$[38]

M	Fathizadeh *et al.*[38]	Present study $f''(0)$	Absolute Differences
0	-1.1486	-1.013671	0.134929
1	-1.5252	-1.419953	0.105247
5	-2.5161	-2.454496	0.061604
10	-3.3663	-3.321629	0.044671
50	-7.1647	-7.14643	0.01827
100	-10.0664	-10.054877	0.011523
500	-22.3901	-22.38803	0.00207
1000	-31.6432	-31.643584	0.000384

4 Conclusion

The discussion presents theoretical analysis for MHD Casson nanofluid flow owing to rapid stretching in an exponentially sheet. Additionally, the impact of activation energy and binary chemical reactions also considered. The MATLAB's bvp4c along with shooting method is utilized to carried out to the numerical solutions. Skin friction coefficient, Nusselt number and Sherwood number are explained through the table. The impact of key parameters on the fluid velocity, temperature and concentrations are as follows. The velocity of the fluid diminished for enhancing Casson fluid parameter (α), Thermal Grashof number (Gm), magnetic parameter (M), inclination angle (β), and porosity parameter (Da). Temperature of the nanofluids enhances for the escalating the value of heat absorption coefficient (Q), Hartmann number (M), Eckert number (Ec), thermophoresis parameter (Nt) and Brownian motion parameter (Nb). An improving the value activation energy parameter E shows an increasing trend of the fluids concentration. The concentration of the fluid diminishes for boosting the Prandtl number (Pr), Lewis number (Le), Eckert number (Ec), Thermophoresis parameter (Nt), heat absorption coefficient (Q), electrical conductivity (σ_1) parameters.

References

1 Arrhenius S, *Lond Edinb Phil Mag*, 41 (1986) 237.
2 Fazal Haq, *et al.*, *Proc Inst Mech Eng: Part A*, 236 (2021) 308.
3 Muhammad J, Hameed M K, Nisar K S & Majeed A H, *Case Stud Therm Eng*, 44 (2023) 102830.
4 Tamizharasi P, Akbar Y, Magesh A, *Archive Appl Mech*, 95 (2025) 72.
5 Azam M & Abbas Z, *Propuls Power Res*, 10 (2021) 383.
6 Priya M & Reddy P B A, *Propuls Power Res*, 13 (2024) 375.
7 Praveen Kumar P, *et al*., *Numer*, *Heat Transf B: Fundam*, 86 (2025) 2075.
8 Magesh A, Tamizharasi P & Kumar P, *ZAMM, ZAMM-Z, Angew Math Mech, 105* (2025) e202400727.
9 Mondal S & Pal D, *Thermal Advances*, 6 (2026) 100098.
10 Reddy K V, Makinde O D & Gnaneswara Reddy, *Indian J Phys*, 92 (2018) 1439.
11 Kumar D, Ramesh K & Chandok S, *Bull Braz Math Soc New Series*, 50 (2018) 515.
12 Hady F M, Mahdy A, Mohamed R A, Ahmed S E & Omima Abo-zaid A, *J Braz Soc Mech Sci Eng*, 41 (2019) 472.
13 Murthy M K, Sreenadh S, Lakshminarayana P & Sucharitha G, *J Nanofluids*, 8 (2019) 1267.
14 Goud B S, Kumar P P & Balga B S, *Partial Differ Eqn Appl Math*, 2 (2020) 100015.
15 Awais M, Raja M A Z, Awan S E, Shoaib M & Ali H M, *Alex Eng J*, 60 (2021) 1355.
16 Das S, Banu A S, Sarkar S, Ali & Jana R N, *ZAMM J Appl Math Mec*, 104 (2023) e202300657.
17 Machireddy G R, Polarapu P & Gorla R S R, *J Nanofluids*, 6 (2017) 71.
18 Vinodkumar Reddy M, Lakshminarayana P, Vajravelu K & Sucharitha, *Numer Heat Transf Part A: Applic*, 86 (2025)1069.
19 Upreti H, Pandey A K, Lingwal S & Bartwal P, *Multidiscip Model*, 21 (2025) 1427.
20 Huang H & Ayoub J, *SPE J,* 13 (2008) 112.
21 Gouran S, Vahidi J, Akbari H & Ghasemi S E, *Case Stud Therm Eng*, 52 (2023) 103753.
22 Kodi R, Ganteda C, Dasore A, Logesh Kumar M, Laxmaiah G, Hasan M A, Islam S & Razak A, *Case Stud Therm Eng*, 44 (2023) 102875.
23 Ahmadi Azar A, Jalili P, Moziraji Z P, Jalili B & Ganji D D, *Heliyon*, 10 (2024) e34888.
24 Iqbal J & Akbar Y, *J Therm Anal Calorim*, 151 (2026) 9753.
25 Akbar Y, Chen C, Iqbal J & Alotaibi H, *Int Commun Heat Mass Transf*, 179 (2026)112085.
26 Magesh A, *et al*., *J Phys: Conf Series*, 1850 (2021) 012111.
27 Zahid U M, Akbar Y & Abbasi F M, *Chin J Phys*, 67 (2020) 330.
28 Noreen S, Farooq U, Liu H, Fatima N, Imran M, *et al.*, *Int Commun Heat Mass Transf*, 169 (2025) 109858.
29 Nadeem S, Noreen Sher Akbar & Rashid Mehmood, *J Magn Magn Mater*, 378 (2015) 457.
30 Tarakaramu N, Satya Narayana P V, Babu D H, Sarojamma G & Makinde O D, *Int J Heat Technol*, 39 (2021) 205.
31 Wahid N S, Arifin N M, Pop I, Bachok N, Hafidzuddin M E H, *Alex Eng J*, 61 (2022) 12661.
32 Ghulam R, Wang X, Yashkun U, Ali L L & Shahzad H, *J Magn Magn Mater*, 571 (2023) 170587.
33 Lund L A, Yashkun U & Shah N A, *J Therm Anal Calorim*, 149 (2024) 2303.
34 Yousuf A M, Rahman M, Ali M M, Ahmmed S F & Haque S, *Int Commun Heat Mass Transfer*, 155 (2024) 107572.
35 Magesh A, *J Nanofluids*, 15 (2026) 69.
36 Riaz A, Shehzadi M, Akram S, Alhamzi G & Mahmoud E E, *Mater Today Commun,* 40 (2014) 109971.
37 Mondal S K & Pal D, *Thermal Adv,* 6 (2026) 100097.
38 Fathizadeh M, Madani M, Khan Y, Faraz N, Yıldırım A & Tutkun S, *J King Saud Univ Sci*, 25 (2013) 107.
39 Shamshuddin M, Sademaki L J, Panda S, Mishra S R, Khan U & Souayeh B, *Nanotechnol*, *Rev*, 14 (2025) 2025.
40 Jawad M, Hameed M K, Nisar K S & Majeed A H, *Case Stud Therm Eng*, 44 (2023)102830.